

Lawrence Berkeley National Laboratory

Lawrence Berkeley National Laboratory

Title

Effect of Saline Waste Solution Infiltration Rates on Uranium Retention and Spatial Distribution in Hanford Sediments

Permalink

<https://escholarship.org/uc/item/27f938x5>

Authors

Wan, Jiamin
Tokunaga, Tetsu K.
Kim, Yongman
et al.

Publication Date

2008-06-03

Peer reviewed

24 formation and accumulation at the neutralized plume front could be one mechanism responsible
25 for highly heterogeneous U distribution observed in the contaminated Hanford vadose zone.

26

27 **Introduction**

28 DOE's Hanford Site is one of the most contaminated nuclear facilities in North America. The
29 tank BX-102 overflowing event in 1951 was reported as the largest and deepest migration of U
30 isotopes in the B-BX-BY Waste Management Area. An estimated 10 tons of U(VI) was
31 discharged into the vadose zone as the result of this single event (1,2). A U plume has been found
32 in the groundwater, north and east of the BX tank farm. Isotopic analyses indicate the U could
33 have originated from this 1951 leakage (3,4). Recently, a high concentration U plume ($U \approx 0.027$
34 M) was detected within the deep vadose zone (80 m) close to the water table, and believed to
35 originate from the BX-102 overfill event (5), suggesting U(VI) is continuing to migrate. The
36 DOE's remediation strategies including long-term stewardship and monitored natural attenuation
37 need to be based on the best understanding of current U spatial distribution, speciation, and
38 future mobility. Gaining the needed understanding is extremely difficult because of the
39 complexity of the strongly coupled hydrological and geochemical processes, sediment
40 heterogeneity, and insufficient historical records. Despite these difficulties, significant progress
41 has been made during the past a few years. Studies conducted on borehole sediment samples
42 collected from beneath BX-102 release site have provided valuable information on U fate and
43 transport in this plume (6). A U solid phase determined to be within the uranyl silicate
44 (uranophane) group, precipitated within microfractures of quartz and feldspar grains, based on X-
45 ray absorption spectroscopy and X-ray diffraction (7), micro-XANES spectroscopy (8), and laser
46 fluorescence spectroscopy (9). Slow dissolution kinetics of these U(VI) silicates from micro-

47 pores within sediment grains and intragranular mass transfer limitations is expected to keep rates
48 of U(VI) release into pore waters very low (10). The intragranular porosity and internal surface
49 area in Hanford sediments is so large that it accounts for most of the moisture and solute storage
50 capacity at the low water contents typical of the Hanford vadose zone (11), and may be effective
51 in immobilizing U(VI) (8). Laser fluorescence speciation of U in pore waters from core samples
52 indicate predominance of $\text{UO}_2(\text{CO}_3)_3^{4-}$ and $\text{Ca}_2\text{UO}_2(\text{CO}_3)_3^0$ (12). In order to study waste stream-
53 sediment reactions and plume geochemical evolution, a plume profiling method was introduced
54 (13), that is capable of providing chemical and physical properties of both pore fluid and
55 sediment at any desired location along a plume.

56 One of the most challenging issues in predicting U fate and transport is to understand the
57 dominant geochemical processes occurred during the initial infiltration of the waste solution into
58 the vadose zone sediment. These early stage processes may have largely determined the current
59 spatial distribution, speciation, and mobility of U. This study is designed to address this issue
60 through laboratory simulations of the Tank BX-102 overflowing event using the column profiling
61 method. We synthesized the waste solution (the solution that was sent to Tank BX-102) based on
62 recipe from historical records. Uncontaminated representative Hanford vadose zone sediment
63 was used to pack the columns. The experimental temperature was controlled at 70°C to simulate
64 the field condition that was heated by radioactive decay. Because flow rates of the waste stream
65 infiltrating into the sediments are unknown and not possible to obtain directly, we chose flow
66 rate as the main variable in this study.

67

68 **Experimental**

69 **Metal Waste Solution.** It is important to recognize that there were no direct measurements or
70 accurate historical records of the chemical compositions of the neutralized metal waste solution
71 (MWS) at the time of the overflow event. For the tank 241-BX-102 overflow in 1951, calculated
72 compositions were based on solubility data for the U phosphate and carbonate solids (because
73 part of the U in the initial neutralized MWS precipitated as U phosphate and U carbonate sludge
74 in the tank prior to and during the accidental overflow), and based on the calculated total loss of
75 MWS from the event. From two different reports (1,2), the calculated MWS at the time of
76 release contained 0.114 and 0.122 M U(VI), 2.1 and 2.92 M sodium, 0.61 and 0.64 M total
77 carbonate, respectively, and 0.53 M nitrate, 0.36 M phosphate, and 0.23 M sulfate, and had pH
78 10.4. The estimated total U loss from the event is 10 metric tons (1,2). We took an
79 experimentally-based approach to synthesize the MWS by going through the historical Pu
80 extraction procedure (excluded the fission products) presented in Serne et al. (14) to obtain an
81 approximate equilibrium partitioning of U between sludge and supernatant. Four steps were
82 involved including metal U storage solution preparation, bismuth phosphate precipitation,
83 centrifugation, and neutralization. After separation of precipitates and neutralizing the liquid
84 phase to the desired pH of 10.4, the final synthesized neutralized MWS contained 0.114 M U,
85 0.75 M total C, 0.34 M P, 0.24 M SO_4^{2-} , 0.87 M NO_3^- , and 3.4 M Na^+ , and had a pH of 10.4 (all
86 values measured). Assuming that 0.34 M of C is associated with U as $\text{UO}_2(\text{CO}_3)_3^{4-}$, that the
87 remaining C occurs as HCO_3^- and CO_3^{2-} in a 0.8:1 ratio at pH 10.4, and HPO_4^{2-} is the dominant P
88 species, the total analyzed anion versus cation charge concentrations are -3.1 M_c and $+3.4 \text{ M}_c$,
89 respectively. These calculations do not account for the effect of high ionic strength on pK_a values

90 of carbonate and phosphate. The synthesized MWS was stable at both room temperature and
91 70°C over the entire period of experimental time.

92

93 **Sediment.** Uncontaminated Hanford formation “coarse sand” was used to pack the columns.
94 This glaciofluvial sediment was collected from the 200 East Area at a depth of about 1.5 to 3 m.
95 Its major components are feldspar, quartz, and basaltic rock fragments. The sediment used in this
96 study contains 93% sand, 6.0% silt, and 1.0% clay. The median grain-size is 350 μm . Calcium
97 carbonate comprises 1.1% of the total mass. The pH measured from a sediment water extract
98 (water to sediment mass ratio = 1:1, at 21°C for 24 hours) was 8.4.

99

100 **Column Profiling Method.** The waste plume formed from the liquid overfilling event was
101 simulated in the laboratory using the column profiling method. Waste solution seepage was
102 simulated in sediment columns that were sectioned after plume migration to a desired distance.
103 Columns used in this study were 0.50 meter long, constructed from 38 mm ID Teflon pipe.
104 Uncontaminated Hanford formation sediment (at the field moisture content of 7.0 mass %) was
105 used to pack the columns homogeneously (dry bulk density $\approx 1.65 \text{ g cm}^{-3}$). Column experiments
106 were conducted at $70 \pm 0.5^\circ\text{C}$ (the estimated elevated temperature caused by decay of other
107 radioactive isotopes not included in our MWS). Three different flow rates were used; 25, 5, and 1
108 cm day^{-1} (pore water velocity). The MWS was injected into the vertically oriented columns, with
109 upward flow in order to avoid gravity induced finger flow. Solutions were supplied using syringe
110 pumps (Harvard Apparatus), with the influent line immersed in the temperature-controlled water
111 bath for thermal equilibration. Flow was terminated at about 30 cm of travel distance before the
112 MWS reached the column outlet in order to capture the entire length of the simulated plume. The

113 column was quickly sectioned, and pore liquids were immediately vacuum extracted through a
114 filter for each sediment segment. Cellulose filter paper of 2 μ m pore size was selected because it
115 permitted rapid filtration. The extracted pore liquids were then used for a variety of analyses.
116 After the extraction, the residual pore liquid was removed from the sediment by applying 20 mL
117 distilled water evenly on the top of the drained sediment (still sitting on the filter paper under
118 vacuum extraction). This procedure for removing pore liquid from each segment took about 2
119 minutes. The sediment segments were then air-dried and used for analyses of the retained
120 amount of U. Analyses of the segment samples of extracted plume liquid and solid sediment
121 permitted construction of chemical profiles along U waste plume paths.

122

123 **Flow Rate Consideration.** Given the importance of pore water velocity on reactive transport,
124 flow rate was a key variable in this study. In many environments, the saturated hydraulic
125 conductivity, K_{sat} , of the sediment provides a reasonable upper limit for waste infiltration rates.
126 However, given the very high K_{sat} of some Hanford formation sands (10^2 to 10^4 m day⁻¹), waste
127 solution seepage probably occurred at lower rates controlled by lower permeability inter-layers
128 and by supply (leakage) rates. Information on the flow rate during the release was not attainable,
129 and to our knowledge, no attempts have been made previously to understand the flow rate effects
130 on U transport through Hanford sediments. Although our tested flow rates (25, 5, and 1 cm day⁻¹)
131 only covered the slower range, results from their general trends can provide useful information.

132

133 **Analytical Methods.** The turbidity and pH of each sediment segment's pore liquid were
134 measured immediately following column sectioning and solution extraction. At the same time,
135 two fractions of each segment pore liquid (including suspended colloids if present) were

136 withdrawn into the prepared carrying solutions for U concentration analyses using KPA-11A
137 (Chemchek, Richland, WA), and for other major elemental analyses using ICP. Carbon was
138 analyzed using a TIC-TOC analyzer (O-I Analytical). The segmented sediment samples were
139 analyzed for U content by gamma spectrometry (Gamma Table Detector, GMX-50220-P, EG&G.
140 Ortec). Morphology, chemical composition, and structure of the colloids in plume front liquid
141 phase were characterized using scanning electron microscopy (SEM), energy-dispersive X-ray
142 spectrometry (EDS), and synchrotron micro-X-ray diffraction (μ XRD) conducted at beamline
143 X26A of the National Synchrotron Light Source. Uranium species in reacted sediment were
144 determined using time-resolved laser fluorescence spectroscopy (TRLFS) conducted at the
145 Environment Molecular Sciences Laboratory (12,15).

146

147 **Results and Discussion**

148 The results presented in this paper are mainly from three columns with three different
149 infiltration flow rates of the synthesized MWS. An additional column run was conducted at the
150 25cm d^{-1} flow rate. However, only U concentration and pH values of the solution phase were
151 analyzed. Additional repetitions were not possible because of expenses associated with
152 synthesizing more MWS.

153 **Plume pH Evolution and Colloid Formation**

154 Accumulation of massive quantities of bright yellow colloids was observed in a very
155 narrow vertical region within the extracted plume liquid phase for columns with higher flow rates
156 ($\geq 5\text{cm d}^{-1}$). Figure 1a is a photograph showing this phenomenon. Each vial contains the
157 extracted liquid in its original order along a plume path. On this figure the flow direction
158 corresponds to the sequence from right to left; displaced native pore water (initial moisture 7.0

159 mass %), plume front, and plume body. Coincident with the location of colloid accumulation,
160 dramatic pH reduction was measured within the plume front region. Figure 1b shows measured
161 plume pH profiles. The pH measurements were performed immediately after extraction of pore
162 solutions, and found to be stable upon later re-measurement. The degree of pH decrease at the
163 plume front was greater at higher flow rate. The pH decreased to as low as 6.4, four units lower
164 than the pH of initial waste solution (pH 10.4), and two units lower than pH value of the native
165 sediment pore water (pH 8.4). The measured pH values of the displaced native soil water were in
166 the range of 7.4 to 8.4 caused by different degrees of diffusive mixing with the more acidic
167 plume front liquid. For the lowest flow rate of 1.0 cm d^{-1} , the sharp pH minimum was lacking,
168 and the front exhibited only a zone of diffusely reduced pH. The longer residence times
169 associated with slower flow rates allowed diffusive mixing to diminish the sharpness of the
170 reaction front. The pH of plume bodies decreased from values near those of the influent at the
171 entry point toward neutral values at the plume front. Because U solubility is least at circum-
172 neutral pH, the pH reduction phenomenon at the advancing plume front must have driven U
173 precipitation (discussed later). Sodium concentration profiles (normalized to the inlet Na
174 concentration of 3.4 M in the MWS) are presented in Figure 1c. Sodium, as the dominant cation
175 in the very saline influent MWS, is a secondary indicator for the extent of the waste plume, but
176 its profile lags behind the plume front primarily because of partitioning onto cation exchange sites.
177 In Figure 1c we see that the plume body has normalized Na concentrations close to one; a plume
178 front region has normalized Na concentrations between zero to one; and a region of displaced
179 native soil water has normalized Na concentrations close to zero. Turbidity values (Figure 1d) are
180 indicators of relative concentrations of suspended colloids. Sharp and high turbidity peaks
181 appeared at the plume front, with the peak values reaching as high as 10,000 nephelometric

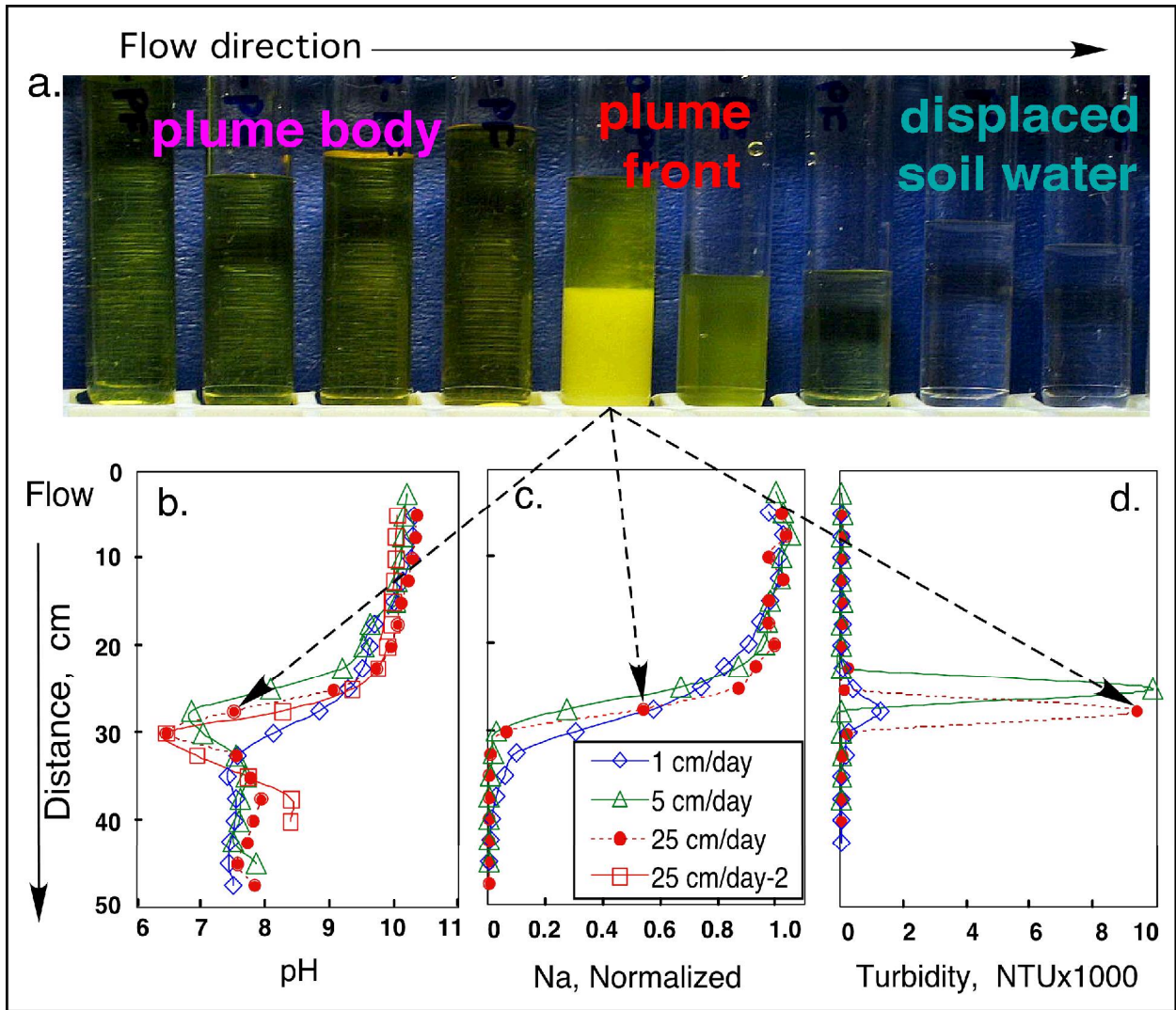
182 turbidity units (NTU). The turbidity peaks do not precisely coincide with the pH minima.
183 Instead, the turbidity maxima reproducibly occurred slightly behind the pH minima. In Figure 1a,
184 the pH of bright yellow colloid-rich vial is 7.5, and its normalized Na concentration is 0.55. The
185 pH minimum of 6.4 is associated with the adjacent downstream sample.

186 The degree of pH decrease and the extent of colloid formation at the plume front are both
187 strongly depend on flow rate. Increased flow rate resulted in larger extent of pH decrease, higher
188 degree of colloid formation, and more U accumulation at the plume front. The general
189 mechanisms for pH decrease and colloid formation at the plume front during infiltration of high
190 salinity solutions were discussed in earlier papers (13,16,17). In brief, it consists two processes.
191 One is cation exchange, with Na^+ as the dominant cation rapidly and completely displacing
192 exchangeable Ca^{2+} and Mg^{2+} from the sediment. As the plume advances, concentrations of these
193 divalent cations build up at the plume front. Greater accumulation of these divalent cations
194 occurs with longer distances of plume migration. The second process is precipitation of
195 supersaturated $\text{Ca}^{2+}/\text{Mg}^{2+}$ -bearing minerals resulting in the observed colloid formation. At the
196 same time, precipitation reactions release protons and drive pH reduction. The pH decrease
197 coincides with greatly decreased solubility of U(VI) minerals (18), hence also drives precipitation
198 of U(VI) colloids.

199

200

201



202

203

204

205

206

207

208

209

210

Figure 1. Plume liquid phase properties along the plume flow path. (a.) Photograph of extracted pore liquid from individual sections of a sediment column, showing large quantity of U-containing colloids formed at a narrow distance at the plume front. (b.) Plume pH profiles, showing large pH decrease at the plume fronts. (c.) Sodium concentration profiles. Indicating vertical distances, the plumes traveled. (d.) Turbidity profiles, showing high turbidity peaks occurred near the plume fronts.

211 Major Chemical Compositions in Plume Liquid Phase

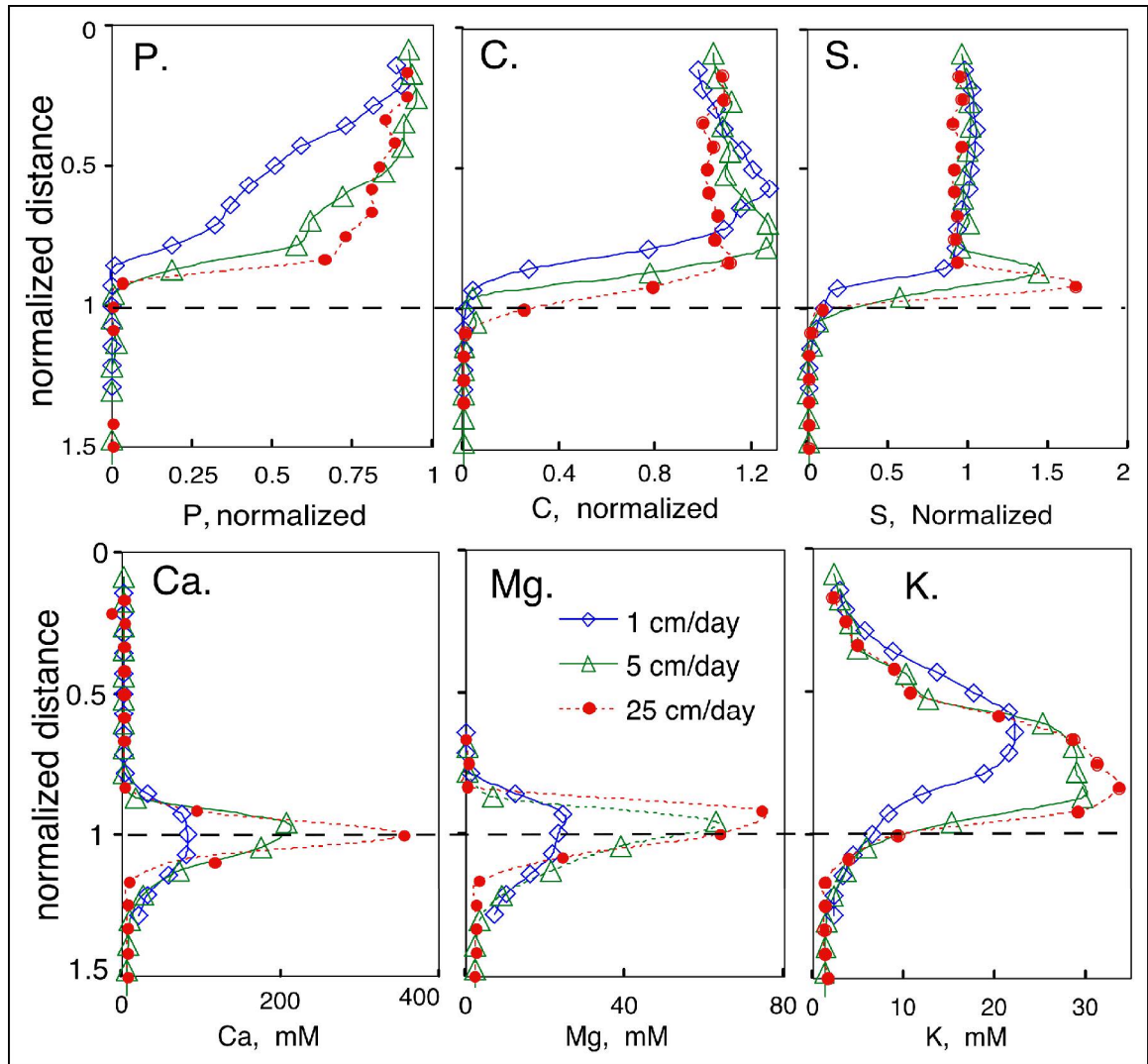
212 The elements Na, K, Ca, Mg, P, and S were analyzed using ICP, with 5% to 10% relative
213 uncertainties determined through duplicated or triplicate runs. The C (carbonate, bicarbonate)
214 concentrations were analyzed using a TIC-TOC analyzer, also with 5-10 % uncertainties
215 determined through duplicated or triplicate runs. The element profiles of extracted plume liquids
216 are presented in Figures 2. Physical distances along the downward flow direction have been
217 normalized to the plume length, defined by the locations of the pH minima (Figure 1b), in order
218 to compensate for small variations in actual plume lengths, and to facilitate comparisons among
219 the different flow rates. Additionally, the measured major anions were normalized to their
220 influent concentrations for easier comparison between initial and reacted concentrations. Because
221 Ca, Mg, Al, and K were not contained in the influent MWS, and came solely from the sediment,
222 their measured concentrations are presented without normalization.

223 The concentration profiles of P, C, and S (the least reactive NO_3^- was not measured) are
224 presented in Figures 2-P, C, and S. Concentrations of HPO_4^{2-} decreased rapidly with depths, and
225 showed greatest loss from solution at the lowest flow rate. For example, at 25 cm of infiltration
226 distance the MWS lost 70% and 35% of its initial HPO_4^{2-} under infiltration rates of 1 and 25 cm
227 d^{-1} , respectively. These losses indicate rapid phosphate precipitation occurred during MWS
228 infiltration. Carbonate profiles show normalized values close to 1.0, and increase with increased
229 depths for two columns, indicating little carbonate loss during reactions. We do not know why C
230 concentrations increase with distance. Sulfate behaved very differently. The SO_4^{2-} profiles were
231 fairly uniform throughout most of the pore solution profiles, with up to about 5% loss from the
232 influent concentration (Figure 5-S.). However, sharp and high SO_4^{2-} peaks (normalized S up to
233 1.6 for the highest flow rate) appeared just behind the plume fronts. The SO_4^{2-} concentration peak

234 was not present under slowest flow rate. Recall that the extracted pore solutions were filtered
235 through 2 μm membranes, which would remove only the larger suspended colloids. A possible
236 mechanism for SO_4^{2-} accumulation just behind the plume front is homogeneous precipitation of
237 SO_4^{2-} -containing gypsum colloids within the Ca-rich plume front. The small lag of the SO_4^{2-}
238 peak relative to that of the plume front Ca^{2+} peak may have resulted from slight retardation of
239 newly formed particles. This possibility is supported by later measured plume front colloids
240 containing dominantly S and Ca using SEM EDS.

241 Sharp peaks of Ca^{2+} and Mg^{2+} were detected at the plume fronts, with concentrations up
242 to hundreds of mM for Ca^{2+} and tens of mM for Mg^{2+} (Figures 2-Ca, Mg). These divalent
243 cations accumulated from Na^+ replacing exchangeable Ca^{2+} and Mg^{2+} from the mineral surfaces
244 of the sediment. The cation exchange capacities for coarse and fine Hanford sands have been
245 reported in the range of 17 to 180 $\text{mmol}_c \text{kg}^{-1}$ (6). In these Hanford sands, Ca^{2+} and Mg^{2+} account
246 for about 80% and 13% of the exchangeable bases, respectively. The observed $\text{Ca}^{2+}/\text{Mg}^{2+}$ spatial
247 distributions not only reflect rapid cation exchange, but diffusion and hydrodynamic dispersion
248 as well. Longer travel times associated with slower flow rates result in more diffuse $\text{Ca}^{2+}/\text{Mg}^{2+}$
249 displacement fronts (13). The enriched K^+ within the plume relative to the displaced soil water
250 resulted mainly from dissolution of K-containing minerals, although native Hanford sediments
251 do have some cation-exchangeable K^+ (Figure 2-K). The broadness of the K^+ -enriched region
252 and its lag behind the sharp Ca^{2+} and Mg^{2+} peaks, reflect slower kinetics of K^+ release through
253 mineral dissolution relative to rapid cation exchange.

254



255

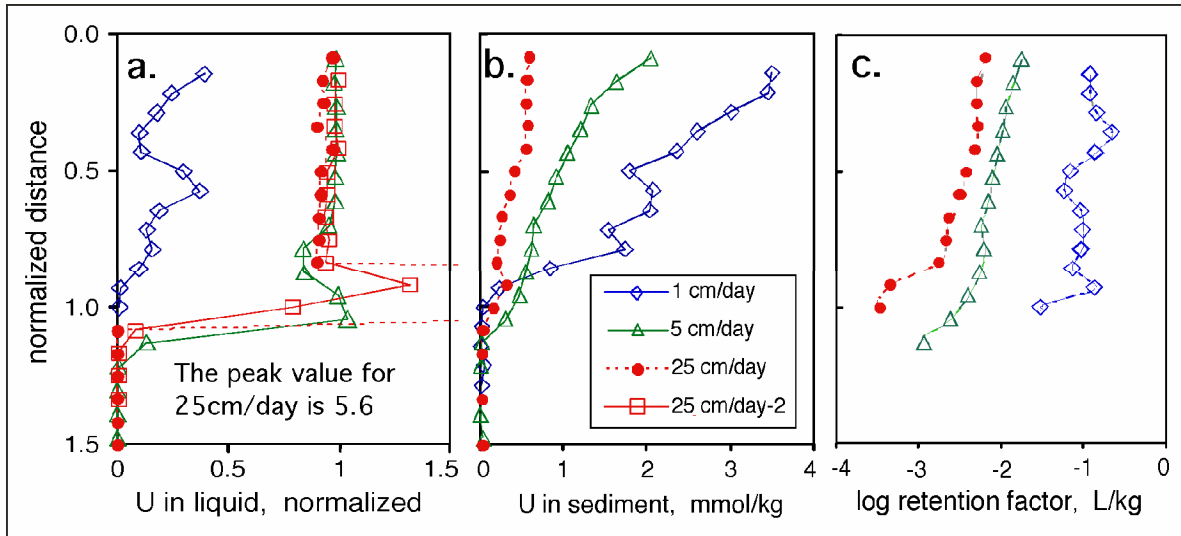
256 **Figure 2.** Concentration profiles of some major ions in the plume liquid phase. The measured
 257 concentration for P, C, and S were normalized to their influent concentrations (0.34M P, 0.75M
 258 C, and 0.24M S) in the initial MWS. The initial MWS did not contain Ca, Mg, and K, and their
 259 only source is the sediment.

260

261 **U Spatial distribution within a plume**

262 The uncertainties in U concentration data were 3-5% for liquid phase analyses using
 263 KPA, and ~20% for sediment using gamma ray spectrometry (triplicates). In the plume body

264 region (Figure 3a), normalized U profiles are close to and slightly reduce from unity for the 5 and
 265 25 cm d⁻¹ flow rates, showing at most about 5% lose of U from the original MWS. This U
 266 depleted from plume body liquid was adsorbed by sediment. For the sediment column infused at
 267 1 cm d⁻¹, normalized U values are ≤ 0.25, indicating >75% of U was retained by the sediment.
 268



269
 270 **Figure 3.** Spatial distribution of U within a plume, showing flow rate effects. (a.) U
 271 concentration profiles in pore liquid phase normalized to the influent U concentration in the
 272 MWS, showing U accumulation at the plume front region under higher flow rates. (b.) U
 273 concentration profiles in the sediment solid phase, and (c.) U ratios of solid-associate U to
 274 solution U, presented as profiles of log₁₀ retention factor.

275
 276 The absolute concentrations of elements in the plume front are highly variable because of
 277 their steep concentration gradients associated with being within a moving reaction front. For
 278 example, in the 5 cm d⁻¹ column, measured geochemical parameters within one of the plume
 279 front segments included pH 7.0, U 124 mM, C 193 mM P 0.2 mM, and S 18 mM. These

280 concentrations are especially transient under rapid flow conditions. If samples were taken at
281 slightly different locations or times, or by using a different filter pore size, different
282 concentrations of these elements would probably have been obtained. However, the data convey
283 the basic message that most of the plume front U was not in complexes with either P or S. More
284 interestingly, from C:U ratio of 1.6 in this particular plume front sample, much of its U was no
285 longer in complexes with carbonate [$\text{UO}_2(\text{CO}_3)_3^{4-}$] as it was originally in the MWS. When the
286 solution pH dropped from 10 to 7.0, U(VI) solubility drops to $\sim 10^{-5}$ M (e.g., schoepite). Thus, the
287 plume front is a moving zone within which the advancing U precipitates. The fact that
288 suspension U concentrations exceed that of the source solution under higher flow rates shows
289 that U precipitation is homogeneous, and that deposition of newly formed U(VI) colloids is
290 kinetically limited.

291 The flow rate-dependence of U transport at the plume front is evident in U liquid phase
292 concentration profiles (Figure 3a). Recall that finer suspended colloids are included in the
293 “solution” phase because 2 μm filters were used. The normalized U concentrations for the two
294 faster flow rate columns are greater than one in the plume front region, indicating local
295 accumulation of suspended U colloids. As mentioned earlier, only pH and liquid phase U
296 concentration data were obtained for the duplicate run 25 cm/day-2. The normalized U
297 concentrations from the second run yielded a lower peak value of 1.38 at the front (Figure 3a)
298 compared to 5.6 for run 25 cm/day-1. Although the U peak value was not quantitatively
299 reproduced, the phenomenon of U accumulation in the plume front was confirmed. As discussed
300 previously, the extremely nonequilibrium conditions make replication of U concentrations within
301 the plume front very difficult. In contrast, slower flow rates permit closer approach to local
302 equilibrium within the plume front, and no U accumulation at the plume front occurred in the 1

303 cm d⁻¹ column. Thus, the extent of U transport reflects complex flow rate-dependent factors
304 including homogeneous colloid formation from highly supersaturated pore liquids, and colloid
305 deposition onto the stationary sediment matrix.

306 U concentrations retained by the sediment solid phase (through sorption and
307 precipitation) are presented in Figure 3b. The U concentrations in sediments at different flow
308 rates were generally inversely related to aqueous phase U profiles in Figure 3a. Slower flow rates
309 resulted in higher sediment-associated U concentrations, reflecting significant rate limitations to
310 sorption and precipitation. Partitioning of U within the plume between the sediment solids and
311 pore liquids was described in terms of a retention factor (L kg⁻¹), obtained by dividing the U
312 concentration measured on the solids by that measured in the associated pore waters (L/kg). The
313 retention factors shown in Figure 3c differ from the conventional retardation factor K_d in that
314 geochemical equilibrium is not assumed, and both sorbed and solid phase U are included in the
315 sediment-associated component. The retention factor is useful because it directly indicates the
316 ratio of relatively immobile U vs. still highly mobile U within the plume. These data show that
317 within the main plume bodies, retention of U in solid phases are ~1.5 order of magnitude higher
318 for the lowest flow rate relative to higher flow rate cases (Figure 3c). The fact that retention
319 factors at the plume fronts are lower, even though this region is lowest in pH and thus most
320 favorable for U sorption and precipitation, is consistent with the presence of significant quantities
321 of suspended U colloids. Kinetic limitations are reflected in the fact that the sediment at the
322 plume front has only been exposed to the U-rich MWS for short times. Note that for the 25, 5,
323 and 1 cm d⁻¹ flow rates, sediments within 1 cm of the advancing front have only been exposed to
324 U for about 1, 5, and 24 hours, respectively. The high Ca²⁺ concentration within the neutral

325 plume front also drives formation of aqueous $\text{Ca}_2\text{UO}_2(\text{CO}_3)_3^0$ complexes (19-21), which
326 diminishes U sorption (21) and enhances U transport (22).

327

328 **Plume Front Colloids**

329 The plume front colloids from the 25cm d^{-1} column at the segment with pH 7.5 were
330 analyzed. SEM images presented in Figure S1a (online Supporting Information, SI) show typical
331 morphologies of the colloids. The size and morphology information suggested that further
332 growth and nucleation of colloids occurred after the pore liquid was extracted, because some
333 particles are larger than the 2 μm pore size of the filter used in the extraction. Chemical
334 compositions of the particles were analyzed qualitatively using energy-dispersive X-ray
335 spectrometry (EDS) in areas of $\geq 1 \mu\text{m}^2$. The major elements within the colloids were identified
336 as Ca, P, U, O, Na, Mg, C, and S (Figures S1b, c, d). Synchrotron X-ray micro-diffraction
337 (μXRD) was used to characterize U-rich crystalline phases of the colloids (Figure S1e). The best
338 XRD fit was obtained with sodium uranyl carbonate $\text{Na}_4(\text{UO}_2)(\text{CO}_3)_3$. Some amorphous or very
339 finely crystalline uranyl oxyhydroxides and calcium uranyl phosphates are present in the colloid
340 phase based on the EDS data. The existence of S-containing colloids is consistent with the
341 previously described accumulation of SO_4^{2-} near the front (Figure 2S).

342

343 **U Retained by the Sediment**

344 Reacted sediment from the 1 cm d^{-1} column was chosen for this study because its
345 sediment retained highest U (Figure 3e). Samples were obtained from two locations within the
346 plume, at normalized distances 0.76 (sample 1cm-11) and 0.50 (sample 1cm-15). Without further
347 treatment, rinsed and air-dried sediment grains were used for SEM, EDS, and fluorescence

348 spectroscopy analyses. The SEM image shows the morphology of the secondary minerals on a
349 grain surface (Figure S2A). The EDS spectrum (Figure S2B) provides the chemical composition
350 of the secondary mineral(s) showing U present with other major elements. Results of laser
351 fluorescence analyses are presented in Figures S2C-E (discussed in the online SI). Through
352 comparison with a set fluorescence spectra of natural uranyl minerals, the spectrum of sample
353 1cm-15 matched that of liebigite $[\text{Ca}_2(\text{UO}_2)(\text{CO}_3)_3]$. An unique match for U species in sample
354 1cm-11 was not obtained because its fluorescence spectrum is similar to the spectra of two
355 standard uranium minerals, phosphuranylite $\{\text{Ca}(\text{UO}_2)[(\text{UO}_2)_3(\text{OH})_2(\text{PO}_4)_2]_2(\text{H}_2\text{O})_{12}\}$ and
356 zellerite $[\text{Ca}(\text{UO}_2)(\text{CO}_3)_2(\text{H}_2\text{O})_5]$. The uranium silicate species boltwoodite $[\text{K}(\text{UO}_2)(\text{SiO}_3\text{OH})$
357 $(\text{H}_2\text{O})_{1.5}]$ was absent in this sample.

358

359 **Implications on Understanding Contaminant U in Hanford Vadose Zone**

360 Several processes demonstrated in these laboratory experiments have direct relevance to
361 U-contaminated sediments such as those at the Hanford 200 Area vadose zone. The pH within
362 an alkaline U plume varied from its waste solution value of 10.4 at the point of discharge, down
363 to ~ 7.0 at the moving front. Peaks of Ca^{2+} and Mg^{2+} concentrations appeared at the plume front
364 as the result of rapid cation exchange from sediments (displacement by Na^+) from the infiltrating
365 waste liquid. These results are consistent with the only available field profile data from borehole
366 299-E33-45 at Hanford tank 241-BX-102. The pH profile from the borehole sediment showed
367 pH values varying from 9.6 to 7.3 downward along the flow path, and the high peak
368 concentrations of Ca^{2+} and Mg^{2+} are also observed in the borehole profiles with a neutral pH (6).
369 The $\text{Ca}^{2+}/\text{Mg}^{2+}$ peaks along with neutral pH may be signatures of a plume front in the field.

370 The neutralized pH caused homogeneous U precipitation, and the formation of suspended
371 U-colloids. The measured U accumulation at the plume front exceed its source level by several-
372 fold under the highest tested flow rate. This process might have been one of the causes for the
373 highly heterogeneous distribution of U within vadose zone waste plumes, such as that
374 characterized by samples from borehole 299-E33-45 at the Hanford Site (6).

375 This work also shows that kinetic limitations on sorption and precipitation permit
376 practically unretarded U transport at flow rates ≥ 5 cm/day. Given the very high K_{sat} of Hanford
377 formation sands (10^2 to 10^4 m day⁻¹), the rates of the initial waste liquid seepage could easily
378 have been higher than 5 cm d⁻¹. Therefore low permeability zones within the sediment might
379 have been most important in slowing transport of high concentrations of U during initial release
380 into the Hanford vadose zone. Predictions based on equilibrium K_d partitioning of U would
381 greatly underestimate the extent of U migration.

382

383 **Acknowledgments**

384 We thank Associate Editor Janet Hering for her careful review and suggestions that made this a
385 better paper. We also acknowledge the anonymous reviewers for their helpful comments.
386 Experimental support by J. Larsen and Y. T. He is gratefully acknowledged. This work was
387 carried out under U.S. Department of Energy Contract No. DE-AC03-76SF-00098. Funding was
388 provided by the U.S. Department of Energy (DOE), Environmental Remediation Science
389 Program (ERSP).

390

391 **Supporting Information Available**

392 Additional materials are presented in Supporting Information via the Internet, including figures

393 showing morphologies, chemical compositions, synchrotron micro-X-ray diffraction pattern of
394 plume front colloids, and SEM, EDS, and fluorescence spectroscopy analyses of sediment retained
395 U species. These information are available free of charge via the Internet at <http://pubs.acs.org>.

396

397

398 **Literature Cited**

399 (1) Jones, T. E.; Simpson, B. C.; Wood, M. I.; Corbin, R. A. Preliminary inventory
400 estimates for single-shell tank leaks in B, BX, and BY tank farms. *CH2M Hill, Hanford Group.*
401 *Inc.: Richland, WA 2001.*

402 (2) Corbin, R. A.; Simpson, B. C.; Anderson, M. J.; Danielson III, W. F.; Field, J. G.;
403 Jones, T. E.; Kincaid, C. T. Hanford soil inventory model (SIM) Rev. 1. *RPP-26744 Rev.0,*
404 *CH2M HILL Hanford Group, Inc. , Richland, WA 2005.*

405 (3) Christensen, J. N.; Dresel, P. E.; Conrad, M. E.; Maher, K.; Depaolo, D. J. Identifying
406 the sources of subsurface contamination at the Hanford Site in Washington using high-precision
407 uranium isotopic measurements. *Environmental Science and Technology* **2004**, *38*, 3330-3337.

408 (4) Dresel, P. E.; Evans, J. C.; Farmer, O. T. Investigation of isotopic signatures for sources
409 of groundwater contamination at the Hanford Site. *PNNL-13763; Pacific Northwest National*
410 *Laboratory: Richland, WA 2002.*

411 (5) McCain, R. G. Gamma and neutron Logs of 299-E33-18. *DOE-EM/GJ1302-2006,*
412 *Stoller Hanford Office, Richland, WA. 2006.*

413 (6) Serne, R. J.; Last, G. V.; Gee, G. W.; Schaefer, H. T.; Lanigan, D. C.; Lindenmeier, C.
414 W.; Lindberg, M. J.; Clayton, R. E.; Legore, V. L.; Orr, R. D.; Kutnyakov, I. V.; Baum, S. R.;
415 Geiszler, K. N.; Brown, C. F.; Valenta, M. M.; Vickerman, T. S. Characterization of vadose

416 zone sediment: Borehole 299-E33-45 near BX-102 in the B-BX-BY waste management area.
417 *PNNL-14083; Pacific Northwest National Laboratory: Richland, WA 2002.*

418 (7) Catalano, J. G.; McKinley, J. P.; Zachara, J. M.; Heald, S. M.; Smith, S. C.; Brown, G.
419 E., Jr. Changes in uranium speciation through a depth sequence of contaminated Hanford
420 sediments. *Environmental Science and Technology* **2006**, *40*, 2517-2524.

421 (8) McKinley, J. P.; Zachara, J. M.; Liu, C.; Heald, S. C.; Prenitzer, B. I.; Kempshall, B. W.
422 Microscale controls on the fate of contaminant uranium in the vadose zone, Hanford Site,
423 Washington. *Geochimica Cosmochimica Acta* **2006**, *70*, 1873-1887.

424 (9) Wang, Z.; Zachara, J. M.; Gassman, P. L.; Liu, C.; Qafoku, O.; Catalano, J. G.
425 Fluorescence spectroscopy of U(VI)-silicate and U(VI)-contaminated Hanford sediment.
426 *Geochimica Cosmochimica Acta* **2005**, *69*, 1391-1403.

427 (10) Liu, C.; Zachara, J. M.; Qafoku, O.; McKinley, J. P.; Heald, S. M.; Wang, Z.
428 Dissolution of uranyl microprecipitates in subsurface sediments at Hanford Site, USA.
429 *Geochimica Cosmochimica Acta* **2004**, *68*, 4519-4537.

430 (11) Tokunaga, T. K.; Olson, K. R.; Wan, J. Moisture characteristics of Hanford gravels:
431 Bulk, grain-surface, and intragranular components. *Vadose Zone J.* **2003**, *2*, 322-329.

432 (12) Wang, Z.; Zachara, J. M.; Yantasee, W.; Gassman, P. L.; Liu, C.; Joly, G. Cryogenic
433 laser induced fluorescence characterization of U(VI) in Hanford vadose zone pore waters.
434 *Environmental Science and Technology* **2004**, *38*, 5591-5597.

435 (13) Wan, J.; Tokunaga, T. K.; Larsen, J. T.; Serne, R. J. Geochemical evolution of highly
436 alkaline and saline tank waste plumes during seepage through vadose zone sediments.
437 *Geochimica Cosmochimica Acta* **2004**, *68*, 491-502.

- 438 (14) Serne, R. J.; Jones, T. E.; Lindberg, M. J.; Schaef, H. T.; K. M. Krupka, K. M.
439 Laboratory Scale Bismuth Phosphate Extraction Process Simulation To Track Fate of Fission
440 Products. *PNNL-14120, Pacific Northwest National Laboratory, Richland, WA* **2003**.
- 441 (15) Wang, Z.; Zachara, J. M.; Mckinley, J. P.; Smith, S. C. Cryogenic laser induced U(VI)
442 fluorescence studies of a U(VI) substituted natural calcite: implications to U(VI) speciation in
443 contaminated Hanford sediments. *Environmental Science and Technology* **2005**, *39*, 2651-2659.
- 444 (16) Wan, J.; Tokunaga, T. K.; Saiz, E.; Larsen, J. T.; Zheng, Z. Colloid formation at waste
445 plume fronts. *Environmental Science and Technology* **2004**, *38*, 6066-6073.
- 446 (17) Wan, J.; Larsen, J. T.; Tokunaga, T. K.; Zheng, Z. pH neutralization and zonation in
447 alkaline-saline tank waste plumes. *Environmental Science and Technology* **2004**, *38*, 1321-1329.
- 448 (18) Langmuir, D. *Aqueous Environmental Geochemistry*; Prentice-Hall: Upper Saddle
449 River, NJ, 1997.
- 450 (19) Bernhard, G.; Geipel, G.; Reich, T.; Brendler, V.; Amayri, S.; Nitsche, H. Uranyl(VI)
451 carbonate complex formation: Validation of the $\text{Ca}_2\text{UO}_2(\text{CO}_3)_3$ (aq.) species. . *Radiochimica*
452 *Acta* **2001**, *89*, 511-518.
- 453 (20) Dong, W.; Brooks, S. C. Determination of the formation constants of ternary complexes
454 of uranyl and carbonate with alkaline earth metals (Mg^{2+} , Ca^{2+} , Sr^{2+} , and Ba^{2+}) using anion
455 exchange method. *Environmental Science and Technology* **2006**, *40*, 4689-4695.
- 456 (21) Zheng, Z.; Tokunaga, T. K.; Wan, J. Influence of calcium carbonate on U(VI) sorption
457 to soils. *Environ. Sci. Technol* **2003**, *37*, 5603-5608.
- 458 (22) Tokunaga, T. K.; Wan, J.; Pena, J.; Sutton, S. R.; Newville, M. Hexavalent uranium
459 diffusion into soils from concentrated acidic and alkaline solutions. *Environmental Science and*
460 *Technology* **2004**, *38*, 3056-3062.

461

462

463 **Brief**

464 Infiltration flow rates of uranium-rich, saline waste solution strongly affect uranium retention

465 and spatial distribution within the Hanford vadose zone sediments.